Monthly Notices
of the
ROYAL ASTRONOMICAL SOCIETY

MNRAS **504,** 723–730 (2021)
Advance Access publication 2021 April 1

doi:10.1093/mnras/stab925

The prospects for observing [O III] 52 micron emission from galaxies during the Epoch of Reionization

Shengqi Yang,[1]★ Adam Lidz[2] and Gergö Popping[3]

[1]*Center for Cosmology and Particle Physics, Department of Physics, New York University, 726 Broadway, New York, NY 10003, USA*
[2]*Department of Physics and Astronomy, University of Pennsylvania, 209 South 33rd Street, Philadelphia, PA 19104, USA*
[3]*European Southern Observatory, Karl-Schwarzschild-Strasse 2, D-85748 Garching, Germany*

Accepted 2021 March 29. Received 2021 March 29; in original form 2020 December 30

ABSTRACT

The [O III] 88 μm fine-structure emission line has been detected into the Epoch of Reionization (EoR) from star-forming galaxies at redshifts $6 < z \lesssim 9$ with ALMA. These measurements provide valuable information regarding the properties of the interstellar medium (ISM) in the highest redshift galaxies discovered thus far. The [O III] 88 μm line observations leave, however, a degeneracy between the gas density and metallicity in these systems. Here, we quantify the prospects for breaking this degeneracy using future ALMA observations of the [O III] 52 μm line. Among the current set of 10 [O III] 88 μm emitters at $6 < z \lesssim 9$, we forecast 52 μm detections (at 6σ) in SXDF-NB1006-2, B14-6566, J0217-0208, and J1211-0118 within on-source observing times of 2–10 h, provided their gas densities are larger than about $n_{\rm H} \gtrsim 10^2$–10^3 cm^{-3}. Other targets generally require much longer integration times for a 6σ detection. Either successful detections of the 52 μm line or reliable upper limits will lead to significantly tighter constraints on ISM parameters. The forecasted improvements are as large as ∼3 dex in gas density and ∼1 dex in metallicity for some regions of parameter space. We suggest SXDF-NB1006-2 as a promising first target for 52 μm line measurements. We discuss how such measurements will help in understanding the mass–metallicity relationship during the EoR.

Key words: galaxies: evolution – galaxies: high-redshift – submillimetre: ISM.

1 INTRODUCTION

Recent ALMA observations of atomic fine-structure emission lines have provided spectroscopic redshifts for galaxies into the Epoch of Reionization (EoR) at $6 < z \lesssim 9$ and started to probe their interstellar medium (ISM) properties (e.g. Willott et al. 2015; Inoue et al. 2016; Marrone et al. 2018). Specifically, these measurements constrain the internal structure, dynamics, ionization state, and gas-phase metallicity in some of the first galaxies. The fine-structure line observations can be further combined with rest-frame ultraviolet (UV) estimates of the star formation rates (SFRs) in these galaxies and infrared (IR) determinations of stellar mass, allowing one to study correlations between gas content and stellar populations into the EoR. These, in turn, give crucial empirical guidance for models of galaxy formation and help to determine the properties of the sources that reionized the Universe.

More specifically, this paper focuses on [O III] fine-structure emission lines from the EoR, which probe the gas-phase metallicity and density in the H II regions in these galaxies. First, these observations help in understanding the chemical enrichment history in early galaxy populations. Furthermore, in lower redshift galaxy samples, there is a well-established correlation between gas-phase metallicity and stellar mass (Lequeux et al. 1979; Tremonti et al. 2004): this is thought to reflect the impact of outflows which drive gas and metals out of the shallow potential wells of low-mass galaxies but have less affect in larger galaxies. The recent [O III] measurements, combined with stellar mass estimates, start to study whether these correlations hold and/or evolve into the EoR (Jones et al. 2020, hereafter Jones 2020). Next, the gas density measurements are relevant for understanding the internal structure and escape fraction of ionizing photons from these galaxies (e.g. Benson, Venkatesan & Shull 2013; Kimm & Cen 2014; Ma et al. 2015; Kimm et al. 2019). The escape fraction plays a critical, yet highly uncertain, role during cosmic reionization.

Thus far, ALMA has detected the [C II] 158 micron emission line and the [O III] 88 micron line from tens of $6 < z \lesssim 9$ galaxies (e.g. Pentericci et al. 2016; Carniani et al. 2017; Laporte et al. 2017; Carniani et al. 2018a, b; Hashimoto et al. 2018, 2019; Smit et al. 2018; Novak et al. 2019; Tamura et al. 2019; Harikane et al. 2020b). Intriguingly, in some cases the [O III] luminosities from this sample exceed those of local galaxies (De Looze et al. 2014) with the same SFRs (Moriwaki et al. 2018). The ratio between the [O III] 88 μm and [C II] luminosity is also larger than in local galaxies (Harikane et al. 2020b). In short, the [O III] 88 μm line is a bright and promising tracer of reionization-era galaxies.

Motivated by the ALMA [O III] 88 μm detections and their future promise, we developed a first-principles analytic model for [O III] emission in Yang & Lidz (2020), (hereafter Yang 2020). We leave the more complex modelling required for studying [C II] emission (e.g. Ferrara et al. 2019; Katz et al. 2019) to future work. The Yang 2020 model determines the [O III] luminosity from galaxies with a given SFR, metallicity, gas density, and ionizing spectral shape. Briefly, in these calculations we first compute the total volume in H II regions across each galaxy and the [O III] fraction within these regions. We then determine the level populations in the different

★ E-mail: sy1823@nyu.edu

fine-structure states and the resulting line luminosities. We cross-checked these calculations against CLOUDY (Ferland et al. 2017) simulations and find that they agree to better than 15 per cent accuracy across a broad range of model parameters. We then applied the model to derive bounds on the gas-phase metallicity and density in the H II regions from the current ALMA sample of 88 μm detections and measurements of their luminosity to SFR. (This is denoted herein as L_{10}/SFR since the 88 μm transition is between the first excited level and the ground state, i.e. it is a $1 \rightarrow 0$ transition).

An important degeneracy is left, however, between the metallicity and gas density from the 88 μm and SFR measurements alone (Yang 2020). At high densities, $n_{\rm H} \gtrsim 10^2$–10^3 cm^{-3}, collisional de-excitations become important and it is impossible to distinguish galaxies with high density and metallicity from those with lower density and metallicity, since the line luminosity drops with increasing density and/or decreasing metallicity. The 88 μm and SFR measurements alone yield only an upper bound on gas density, $n_{\rm H}$, and a lower bound on metallicity, Z.

Previous work suggests that future ALMA measurements of the [O III] 52 μm transition may help to break this degeneracy (Jones 2020; Yang 2020). This line arises from transitions between the second excited and first excited fine-structure levels in [O III] (and so the luminosity in this line is denoted hereafter as L_{21}). As noted in these previous studies, the ratio between the 52 and 88 μm emission (L_{21}/L_{10}) provides a powerful *density diagnostic* (e.g. Draine 2011), since the lines have different critical densities and their ratio hence depends on the importance of collisional de-excitations. As the energy splitting between these fine-structure states is small compared to the temperature of the H II region gas, the line ratio is insensitive to the temperature of the gas. Further, the lines arise from the same ion and so the ratio does not depend on the ionization state of the gas, nor appreciably on its metal content.

Jones 2020 also considered the prospects for detecting 52 μm emission with ALMA from some of the current sample of [O III] 88 μm emitting galaxies at $6 < z \lesssim 9$, finding that some of these sources are detectable in reasonable observing times. Here, we extend the work in these previous studies to forecast the quantitative improvements on the gas density and metallicity error bars that will be enabled by new 52 μm measurements in the future. Furthermore, we consider the implications of these improvements for our understanding of the mass–metallicity relationship during the EoR, building off of the earlier work on using the [O III] 88 μm line to constrain this important correlation in Jones 2020 and our previous analytic model in Yang 2020.

The plan of this paper is as follows. In Section 2, we describe the current 10 ALMA [O III] targets at $6 < z \lesssim 9$. Section 3 reviews the [O III] 88 and 52 μm analytic model introduced in Yang 2020. In Section 4, we consider the $n_{\rm H} - Z$ parameter space allowed by current L_{10}/SFR observations and compute the range of observing times required to achieve $6-\sigma$ 52 μm detections using the ALMA sensitivity calculator. In Section 5, we perform Monte Carlo Markov Chain (MCMC) calculations to quantify the parameter space improvements expected towards four promising 52 μm targets. We show that both successful detections and upper limits on the 52 μm signal will significantly tighten the gas density posteriors and also bring stronger constraints on the ISM metallicities. We compare the ISM metallicity constraints from Jones 2020 and Yang 2020, and the future improvements enabled by joint [O III] 88 and 52 μm fits in Section 6. We discuss how these observations can advance our understanding of the mass–metallicity relationship during the EoR. We conclude in Section 7.

2 DATA

We consider the sample of nine ALMA [O III] 88 μm detections plus one upper limit at $6 < z \lesssim 9$, published in the current literature, and summarized in Table 1. These include one gravitationally lensed galaxy at $z = 9.1$ (Hashimoto et al. 2018) (MACS1149-JD1), a lensed Y-band drop-out galaxy A2744_YD4 at $z \sim 8$ (Laporte et al. 2017), and the $z \sim 8$ Y-dropout Lyman-break galaxy (LBG), MACS0416_Y1 (Tamura et al. 2019). At $z \sim 7$, [O III] from one Ly α emitter is detected in a follow-up measurement carried out by Inoue et al. (2016). In addition, the LBG B14-65666 is measured by Hashimoto et al. (2019), and the star-forming galaxy BDF-3299 is detected in Carniani et al. (2017), each near $z \sim 7$. Three luminous LBGs, J1211-0118, J0235-0532, and J0217-0208, at $z \sim 6$ are presented by Harikane et al. (2020a). The galaxy SFRs summarized in Table 1 can also be found in Harikane et al. (2020a). We use the Salpeter IMF based results from this study, rather than the ones in Harikane et al. (2020b) which assume a Charbier IMF, for consistency with our model. Finally, a non-detection of [O III] from the Ly α-emitting galaxy z7_GSD_3811 at $z = 7.7$ is reported in Binggeli et al. (2021).

3 MODEL

Our aim is to forecast the expected SNR for 52 μm emission line observations of this sample of galaxies as well as the improvements expected for the ISM parameter constraints. In order to do this we need to account for current uncertainties in the [O III] 88 μm luminosities and SFRs, and we also need to span the allowed ISM parameter space.

To accomplish this, we turn to the Yang 2020 [O III] emission model. In brief, this model treats the ionizing output of each galaxy as concentrated into a single effective source of ionizing radiation at the centre of a spherically symmetric H II region, which is in photoionization equilibrium. The rate of hydrogen-ionizing photons emitted by this source is given by $Q_{\rm H\,I}$ and is determined by the galaxy's SFR, stellar metallicity, and IMF. Although in reality the [O III] emission arises from a complex ensemble of discrete H II regions distributed across the galaxy, our simplified treatment – with a single effective H II region – should provide an accurate prediction of the total [O III] luminosity summed over all of the H II regions in the galaxy. We adopt a STARBURST99 population synthesis stellar spectrum (Leitherer et al. 1999) with a continuous SFR, a Salpeter IMF (Salpeter 1955), and an age of 10 Myr throughout, in which case the doubly ionized oxygen fraction is close to unity throughout the H II region for the SFRs considered here. As discussed in Yang 2020, we do not expect the precise choice of stellar spectrum here to significantly impact our results. For simplicity in making our forecasts we ignore variations in the gas density and metallicity across each galaxy (see Yang 2020 for extensions to this and further discussion). In this case the gas density is characterized by a single number, $n_{\rm H}$, across each galaxy, while the metallicity is described by the parameter Z.

For simplicity, our baseline model assumption is that the stellar metallicity matches the gas-phase metallicity. Note, however, that Steidel et al. (2016) find evidence for supersolar oxygen to iron abundance ratios in $z \sim 2$–3 LBGs and argue that this is a natural consequence of chemical enrichment dominated by core-collapse supernovae, as would also be expected at the $z \geq 6$ redshifts in our sample. Since iron largely controls the stellar opacity and mass-loss, this case can be roughly described by adopting a lower stellar metallicity for a given gas-phase metallicity. To account for this, we therefore consider also an alternate case in which the stellar

Table 1. Summary of the ALMA high-redshift [O III] galaxies studied in this work and the prospects for future 52 μm detections. The columns in the table give: (1) Object names. (2) Redshifts determined from Lyman-α, the Lyman break, rest-frame UV absorption lines, [C II] 158 μm, or [O III] 88 μm. (3) The total SFRs inferred from UV and IR luminosities. (4) Stellar mass inferred from SED fits or UV magnitudes. The stellar mass of BDF-3299 is determined in Mancini et al. (2015). The stellar masses of J0217-0208, J0235-0532, and J1211-0118 are estimated through an empirical stellar mass versus UV magnitude relationship for $z \sim 6$ LBGs (Song et al. 2016). Other stellar mass references are provided in column (10). (5) [O III] 88 μm luminosities. (6) The ALMA frequency bands capturing the redshifted 52 μm emission line from each galaxy. (7) The range of [O III] 52 to 88 μm luminosity ratios allowed by the L_{10}/SFR measurements. (8) The 1σ noise on the 52 μm (velocity-integrated) luminosity for a 10-h on-source ALMA measurement. (9) The on-source observing time required to achieve an SNR = 6 [O III] 52 μm detection. The first, second, and third entries correspond to the observing time under the maximum, average, and minimum L_{21}/L_{10} cases. (10) References for the [O III] 88 μm measurements, the SFR, and stellar masses. H18: Hashimoto et al. (2018), L17: Laporte et al. (2017), T19: Tamura et al. (2019), I16: Inoue et al. (2016), H19: Hashimoto et al. (2019), C17: Carniani et al. (2017), H20: Harikane et al. (2020b), B20: Binggeli et al. (2021).

Name (1)	Redshift (2)	$\frac{\mathrm{SFR}}{[\mathrm{M_\odot\,yr^{-1}}]}$ (3)	log $\frac{M_*}{[M_\odot]}$ (4)	$\frac{L_{10}}{[L_\odot]}$ (5)	Band (6)	$\frac{L_{21}}{L_{10}}$ (7)	$\frac{\sigma_{L_{21}}}{[L_\odot]}$ (8)	Observing Time/[h] (9)	Ref (10)
MACS1149-JD1	9.110	$4.2^{+0.8}_{-1.1}$	$9.03^{+0.17}_{-0.08}$	(7.4 ± 1.6)E7	–	2.33,0.56	–	Not Observable	H18
A2744-YD4	8.382	$20.4^{+17.6}_{-9.5}$	$9.29^{+0.24}_{-0.18}$	(7.0 ± 1.7)E7	9	5.79,0.58	5.2E8	5.9E2,2.0E3,5.9E4	L17
MACS0416-Y1	8.312	$57.0^{+175.0}_{-0.2}$	$8.38^{+0.11}_{-0.02}$	(1.2 ± 0.3)E9	9	5.23,0.55	3.2E10	9.4E3,3.1E4,8.5E5	T19
SXDF-NB1006-2	7.215	193^{+155}_{-92}	$8.54^{+0.79}_{-0.22}$	(9.9 ± 2.1)E8	9	4.75,0.57	3.2E8	1.73,5.51,1.2E2	I16
B14-65666	7.168	200^{+82}_{-38}	$8.89^{+0.05}_{-0.04}$	(3.4 ± 0.4)E9	9	2.56,0.56	8.4E8	3.35,9.01,69.95	H19
BDF-3299	7.109	5.7	9.3 ± 0.3	(1.8 ± 0.2)E8	9	1.28,0.55	3.6E8	8.7E2,1.7E3,4.7E3	C17
J0217-0208	6.204	153	10.36 ± 0.36	(8.5 ± 2.0)E9	10	0.86,0.54	1.2E9	9.26,13.98,23.49	H20
J0235-0532	6.090	86	10.36 ± 0.36	(3.8 ± 0.3)E9	10	0.90,0.55	1.4E9	60.06,92.56,1.6E2	H20
J1211-0118	6.029	136	10.61 ± 0.36	(4.8 ± 0.7)E9	10	1.32,0.55	8.7E8	6.84,13.64,39.42	H20
z7_GSD_3811	7.664	>8.4	>8.20	<1.6E8	10	7.16,0.56	<2.2E8	>13.90, >47.83, >2.3E3	B20

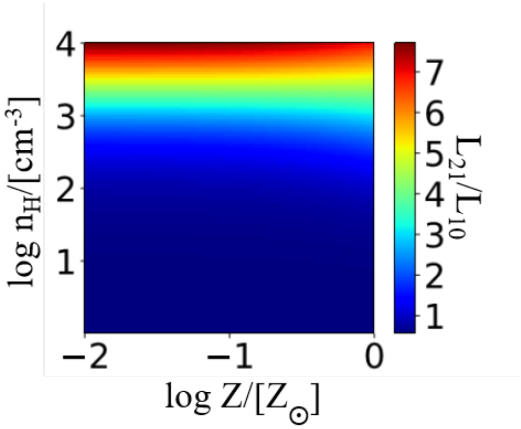

Figure 1. The luminosity ratio in the 52 to 88 μm lines for different gas densities and metallicities. The ionizing photon rate is fixed at $Q_{\mathrm{H\,I}} = 10^{54}$ s^{-1} (expected for an SFR of roughly ∼10 M$_\odot$ yr^{-1}) and the gas temperature is set to $T = 10^4$ K here. The line ratio provides a density indicator.

metallicity is a factor of 5 smaller than the gas-phase metallicity. The reduced stellar metallicity in this scenario increases the ionizing photon output for a given SFR, and thus enhances the [O III] emitting volume, relaxing the gas-phase metallicity bound from the L_{10}/SFR measurements (see Yang 2020 and further discussion below).

The Yang 2020 model then solves for the fine-structure level populations in the three-level atom approximation, accounting for radiative de-excitations, collisional excitations and de-excitations, and subdominant radiative trapping effects (computed in the escape probability approximation; these effects are unimportant for plausible [O III] velocity distributions).

Under these assumptions, the luminosity in the [O III] 88 μm line (L_{10}) and the 52 μm luminosity (L_{21}) may be written as

$$L_{ij} = \frac{R_i}{1+R_1+R_2}\left(\frac{n_{\mathrm{O}}}{n_{\mathrm{H}}}\right)_\odot \frac{Z}{Z_\odot}\frac{A_{ij}}{1+0.5\tau_{ij}} h\nu_{ij}\frac{Q_{\mathrm{H\,I}}}{\alpha_{\mathrm{B,H\,II}} n_{\mathrm{e}}}. \quad (1)$$

Here, R_i is the fractional abundance of O III ions in the i-th energy state and $(n_{\mathrm{O}}/n_{\mathrm{H}})_\odot = 10^{-3.31}$ is the solar oxygen to hydrogen abundance ratio. The quantity A_{ij} is the Einstein-A coefficient, specifying the spontaneous decay rate from the i-th to the j-th energy level. The optical depth, τ_{ij}, is treated self-consistently in the escape probability approximation but is unimportant in practice. Here, ν_{ij} is the rest-frame frequency of the corresponding [O III] emission line, $\alpha_{\mathrm{B,H\,II}}$ is the case B recombination rate of hydrogen, and n_{e} is the number density of free electrons. This formula then connects the luminosity in each line to the ISM parameters, n_{H} and Z.

Yang 2020 used this analytic model to constrain the ISM properties of nine ALMA targets with L_{10}/SFR observations. As discussed earlier, this left a degeneracy between gas density and metallicity. This can be broken by adding [O III] 52 μm measurements, owing to the different critical densities of the two lines. It is instructive to examine the asymptotic behaviour of the line ratio, as discussed in Yang 2020:

$$\frac{L_{21}}{L_{10}} = \begin{cases} \dfrac{k_{02}}{k_{01}+k_{02}}\dfrac{\nu_{21}}{\nu_{10}} \approx 0.55 & \text{if } n_{\mathrm{e}} \to 0; \\ \dfrac{g_2}{g_1}\dfrac{A_{21}}{A_{10}}\dfrac{\nu_{21}}{\nu_{10}} = 10.71 & \text{if } n_{\mathrm{e}} \to \infty, \end{cases} \quad (2)$$

where $g_2 = 5$ and $g_1 = 3$ are the degeneracies of the ^{3}P$_2$ ('2') and ^{3}P$_1$ ('1') levels. The ks are O III collisional excitation rates. The low-density limit has a slight temperature dependence, but this is weak since the energy separation between these states is small relative to the H II region temperature. The number given in equation (2) assumes a gas temperature of $T = 10^4$ K. To further illustrate, Fig. 1 shows the line ratio across the $\log n_{\mathrm{H}} - \log Z$[1] parameter space assuming $Q_{\mathrm{HI}} = 10^{54}$ s^{-1} and $T = 10^4$ K. The luminosity ratio transitions between the low- and high-density limits of equation (2) with a relatively sharp increase in the range $10^2 \lesssim n_{\mathrm{H}} \lesssim 10^3$ cm^{-3}, above which the 52 μm line is more luminous. The ratio is almost independent of metallicity, with only a weak dependence from the fact that the number density of free electrons depends slightly on Z. There is also a small effect that arises because the gas temperature depends on metallicity (see Yang 2020 Eq 2); this is not captured in Fig. 1, which adopts a fixed temperature, but is included in our modelling.

[1]In this work log denotes a base-10 logarithm.

Using the $n_{\rm H} - Z$ constraints in Yang 2020, determined from the L_{10}/SFR measurements in the literature, we identify the currently allowed range in L_{21}/L_{10} for each of the 10 ALMA galaxies. The maximum and minimum values of L_{21}/L_{10} allowed at 68 per cent confidence after spanning the $n_{\rm H} - Z$ parameter space are given in column (6) of Table 1 for each target. In the alternate case, motivated earlier, that the stellar metallicity ($Z_\star$) is 0.2 times the gas-phase metallicity (Z), the higher rate of ionizing photon production in this scenario increases the L_{21}/L_{10} upper bounds by 5 per cent–28 per cent, depending on the target.

4 OBSERVING TIME

We now turn to compute the expected SNR for future ALMA 52 μm observations. We determine the ALMA sensitivity for a 10-h measurement as well as the on-source observing time required to achieve an SNR = 6 [O III] 52 μm detection at peak flux density for each target under different L_{21}/L_{10} scenarios. Specifically, we consider the minimum and maximum L_{21} allowed by the Yang 2020 constraints at 68 per cent confidence, as well as an average between these two luminosity limits.

In order to compute the ALMA sensitivity for each of the 10 targets in Table 1, we use the ALMA Sensitivity Calculator web interface. We assume a Gaussian line profile for each emission line and that the full width at half-maximum (FWHM) of the 52 μm line matches the best-fitting observational line width of its 88 μm counterpart. We adopt the 43 ALMA antenna configuration and frequency channels of width set by the FWHM/3, such that each spectral line is resolved by three channels. We furthermore assume that the angular size of the target is smaller than the beam of the observations, i.e. that the observations do not resolve the target. For simplicity we set the declination as zero for all of the sources. The ALMA band containing the 52 μm line for each target is listed in column (5) of Table 1. The resulting 1σ noise on the integrated 52 μm luminosity for a 10-h on-source measurement is given in column (7). Finally, the on-source integration times required for 6σ detections are shown for the maximum, mean, and minimum L_{21} cases in column (8). As mentioned in Section 3, decreasing $Z_\star$ at fixed gas-phase metallicity increases L_{21}/L_{10} and so shorter integration times are required for 52 μm detections in this case. We are therefore providing conservative detection time estimates.

Among the 10 targets studied in this work, the 52 μm line emitted by MACS1149-JD1 is not observable by ALMA because its observed 52 μm frequency falls in the gap between the band 8 and band 9 windows. The other nine targets are in principle observable. The atmospheric opacity is, however, very large at the observed frequencies of the 52 μm line for A2744-YD4, MACS0416-Y1, and BDF-3299 and so it is not feasible to detect these objects in practice. If the galaxies in this data set tend to have high gas densities, $n_{\rm H} \gtrsim 10^2$–10^3 cm^{-3}, then the [O III] 52 μm lines from SXDF-NB1006-2, B14-65666, J0217-0208, and J1211-0118 can be detected within 10 h, in agreement with the earlier work of Jones 2020. As noted in Jones 2020, modelling of [O II] and [S II] doublet emission lines in the spectra of LBGs at $z \sim 2$–3 indicates gas densities in the $n_{\rm H} \sim$ 200–300 cm^{-3} range (Sanders et al. 2016; Steidel et al. 2016; Strom et al. 2017). If the ALMA galaxies are similar, or still more dense – as one might expect for galaxies at higher redshifts – then this bodes well for detecting their 52 μm emission. [2]

At low gas densities, the 52 μm emission line is significantly harder to detect and it may be possible to place only upper limits on the luminosity of this line. Nevertheless, even in the low-density case where the 52 μm line is almost a factor of 2 less luminous than the 88 μm emission, J0217 is still theoretically detectable within 24 h of on-source integration time. In the intermediate-density case (where we take $L_{21} = L_{10} \times ((L_{21}/L_{10})_{\rm max} + (L_{21}/L_{10})_{\rm min})/2$), we find that 6σ detections are possible in less than 10 h for SXDF-NB1006-2 and B14-65666. In the high- and intermediate-density cases, SXDF-NB1006-2 requires the least time for a significant detection (∼2–6 h). We therefore suggest SXDF-NB1006-2 as a promising first target for an ALMA 52 μm follow-up measurement.

5 52 μM MEASUREMENT AND ISM PARAMETER CONSTRAINTS

Fig. 2 shows forecasts for how the parameter constraints in the $\log n_{\rm H} - \log Z$ plane will improve after including L_{21}/L_{10} measurements. Specifically, we select the four most promising targets from Table 1: SXDF-NB1006-2, B14-65666, J0217-0208, and J1211-0118 and consider 10 h on-source integration times for the 52 μm follow-up observations (see column 7 of Table 1 for the resulting noise estimates.) These forecasts are combined with the constraints obtained in Yang 2020 from the L_{10}/SFR measurements of Harikane et al. (2020a) (grey regions in the figure). In each case, we adopt a hard metallicity prior enforcing $Z \leq Z_\odot$.

As in the previous section, we explore the constraints expected for three different assumptions regarding the line ratio L_{21}/L_{10}. We assume a Gaussian likelihood for the line ratio, the standard error propagation formula to compute the uncertainties on this ratio from the independent luminosity measurement errors, and MCMC calculations to forecast the expected parameter constraints. The top row of Fig. 2 shows the maximal case, the middle row the intermediate scenario, and the bottom row gives the minimum line ratio model calculations. The forecasted constraints from the line ratio alone are shown by the red regions/lines in Fig. 2, while the combined constraints are given in blue. The variations from bottom to top correspond to increasing the gas density in the ISM, as discussed earlier and indicated by the yellow arrow in the figure.

As noted previously, the L_{10}/SFR measurements alone leave a strong degeneracy between gas density and metallicity, giving rise to the 'L'-shaped grey regions in the figure. The 52 μm line ratio measurements will add nearly horizontal ellipses in the $\log n_{\rm H} - \log Z$ plane through their sensitivity to the gas density. The three cases show the impact of shifting the fiducial gas density from a higher value to a lower value as one moves from the top row to the bottom one. Note that in some examples these constraint forecasts come only from upper limits on the 52 μm line emission: for the minimum L_{21}/L_{10} case we do not expect 6σ line detections towards any of the four targets in less than 10 h. Further, for the intermediate L_{21}/L_{10} model, J0217-0208 and J1211-0118 still fall below the SNR = 6 threshold. Those examples illustrate that even an upper limit will help to constrain the parameter space here.

In most cases, we forecast that the gas density posteriors will tighten significantly after including 52 μm follow-up measurements.

[2]The listed times are on-source observing times only, ignoring the calibration overheads. Furthermore, observations in ALMA band 9 and 10 require excellent weather conditions with good phase-stability. In practice, the effective band 9 and 10 observing time per local siderial time hour is limited to just a few hours per ALMA configuration. This is especially true for the compact configurations offered in Cycle 8 2021, the configurations most suitable for a detection experiment.

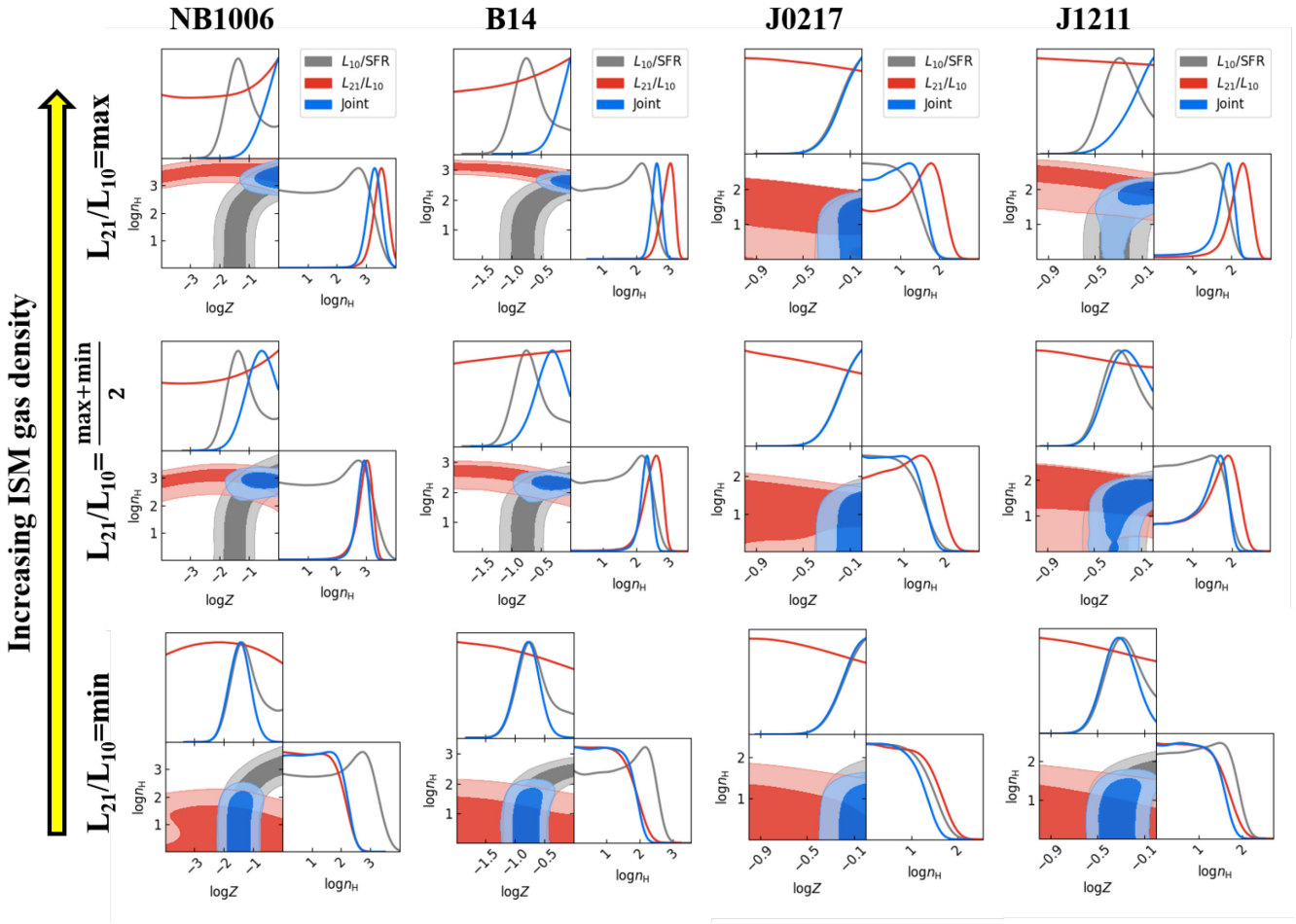

Figure 2. Forecasted improvements on gas density-metallicity parameter constraints from combining current L_{10}/SFR measurements with upcoming redshifted 52 μm observations in four example galaxies, SXDF-NB1006-2, B14-65666, J0217-0208, and J1211-0118 (see Table 1). In each panel, the grey regions and lines show the constraints from the current L_{10}/SFR measurements, the red regions and lines show forecasts for the 52 μm line detections alone, and the blue regions and lines give the joint constraints that will be possible. The upper, middle, and lower rows show results for the maximum, average, and minimum L_{21} scenarios (see text). The shaded regions give 68 per cent and 95 per cent confidence intervals.

In many of the examples shown this should also help to tighten the metallicity constraint by breaking the degeneracy between density and metallicity. For instance, in the maximal line ratio case it will be possible to decisively show that SXDF-NB1006-2 has a high metallicity $Z \geq 0.092Z_{\odot}$ at 95 per cent confidence, while based on L_{10}/SFR alone this galaxy's metallicity may be as low as $Z = 0.011Z_{\odot}$, again at 95 per cent significance. The improvements forecast are weakest for the case of J0217-0208. This galaxy has a very large L_{10}/SFR and so high densities are already excluded for this system (at least under our $Z \leq Z_{\odot}$ prior). Nevertheless, we expect the gas density determination to improve for this galaxy although the metallicity constraint will not tighten. Overall, the prospects for obtaining more stringent ISM parameter constraints from 52 μm observations towards several of the galaxies in the current sample appear promising. In addition, we expect that further 88 μm detections will extend the list of promising targets here in the near future.[3]

[3]For example, the ALMA Large Program REBELS (2019.1.01634.L) aims to discover the most luminous [C II] and [O III] galaxies in the EoR.

6 52 MICRON MEASUREMENTS AND THE MASS–METALLICITY RELATION

The previous section shows that 52 μm measurements can help sharpen constraints on the gas density and metallicity. Here, we turn to further explore the potential scientific impact of these measurements, by quantifying the improvements that will be possible in our understanding of the mass–metallicity relationship during the EoR. This will extend the work of Jones 2020, which started to constrain this important relationship from the current [O III] 88 μm measurements. As mentioned in the Introduction, the improved gas density limits may also help in understanding the escape fraction of ionizing photons. Exploring this, however, will likely require comparison with detailed radiation-hydrodynamical simulations capable of modelling the escape fraction and its dependence on galaxy properties, and so we defer this to possible future work.

The top left panel of Fig. 3 compares empirical fits to the mass–metallicity relationship at lower redshifts and a fitting formula from a current simulation in the literature, along with the 88 μm based metallicity determinations from each of Jones 2020 and Yang 2020 at $6 < z \lesssim 9$. More specifically, the best-fitting empirical $Z(M_*)$ relationships at $z \sim 0$ and $z = 3.5$ from Maiolino et al.

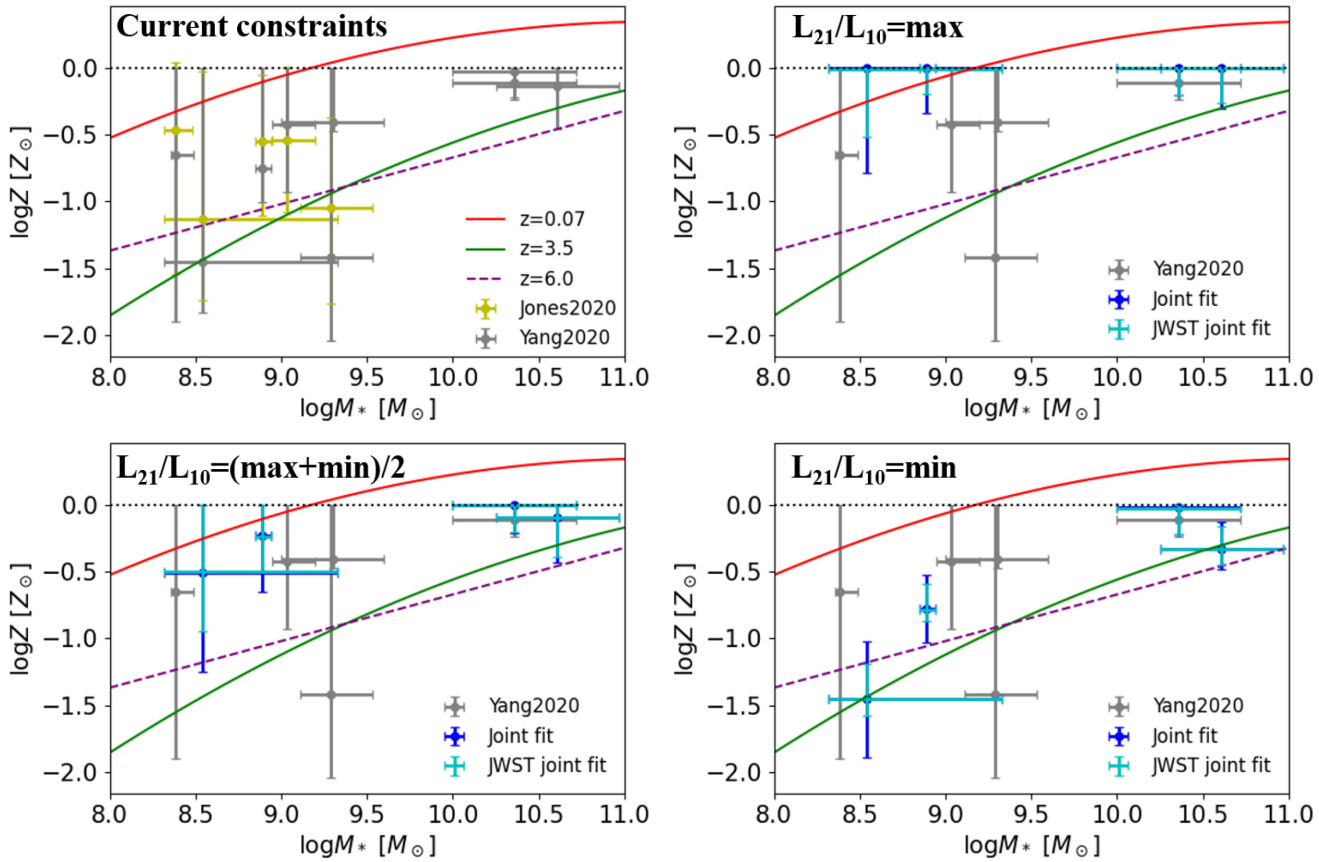

Figure 3. Constraints on the mass–metallicity relationship from Jones 2020 and Yang 2020, compared with results from simulations and observations in the literature. In each panel, the mass–metallicity evolution from $z \sim 0$ to $z \sim 4$ determined empirically by the AMAZE project (Maiolino 2008) is shown (two thin curves at $z = 0.07$ and $z = 3.5$.). The results from the FIRE simulation suite (Ma 2016) at $z = 6$ are given by the purple dashed line. In each panel, the black dotted line at solar metallicity indicates the metallicity prior adopted in Yang 2020 and this work. *Top left*: The metallicity constraints from Jones 2020 and Yang 2020 are shown as yellow and grey crosses, respectively. The other three panels illustrate how the error bars in the mass–metallicity plane may tighten with the addition of 52 μm measurements. The top right, bottom left, and bottom right panels correspond to the maximum, average, and minimum L_{21} scenarios (see text). In each case, we show results for NB1006, B14, J0217, and J1211, identified as promising targets in the previous section, in blue crosses. The cyan points further show improvements that may be possible with upcoming JWST SFR measurements, provided the resulting L_{10}/SFR errors become dominated by the uncertainties on L_{10} alone. Metallicity constraints for JD1, YD4, Y1, BDF, and J0235 from Yang 2020 are shown in grey crosses (these galaxies are less promising for follow-up 52 μm measurements.) All of the error bar in this figure are $1-\sigma$ uncertainties.

(2008) (hereafter Maiolino 2008) are shown in solid curves. These are compared to results from the FIRE simulations (dashed line), calibrated from simulated galaxies at $z = 6$ (Ma et al. 2016) (hereafter Ma 2016). Note that the Ma 2016 $Z(M_*)$ fitting formula predicts a drop of only 0.05 dex between $z = 6$ and $z = 9$; this estimate requires extrapolating their formula beyond the redshift range in which it was calibrated, at $z \leq 6$, out to the highest redshift ($z \sim 9$) in the current ALMA sample. Hence the evolution across the redshifts of this data set is expected to be negligibly small compared to present and upcoming measurement errors.

The current $6 < z \lesssim 9$ metallicity constraints from Jones 2020 and Yang 2020, along with the stellar mass measurements in Table 1, are given by the yellow and grey points, respectively, each with $1-\sigma$ error bars. As discussed further in Yang 2020, these two studies agree despite different methodologies, although the error bars in the Yang 2020 work are larger, given the more agnostic prior on density adopted in that work. Note also that the sample considered in Yang 2020 includes additional galaxies beyond those in Jones 2020: BDF-3299, J0217-0208, J0235-0532, and J1211-0118.

In order to quantify the constraints on the mass–metallicity relation from Jones 2020 and Yang 2020, we calculate the reduced χ^2 difference between the measurements and model $Z(M_*)$ relationships. In doing so, it is important to account for the intrinsic galaxy-to-galaxy scatter in this relationship, which is not well characterized in the current AMAZE observations of Maiolino 2008 nor in the FIRE simulations of Ma 2016. We therefore adopt an intrinsic scatter of $\sigma^{\rm int} = 0.2$ dex based on results from another simulation study, using the IllustrisTNG simulations (Torrey et al. 2019). Specifically, we denote the metallicity measurements towards the ith galaxy by Z_i and the corresponding metallicity error as $\sigma_i^{\log Z}$. The fitted Maiolino 2008 and Ma 2016 $Z(M_*)$ relations are labelled as $\log Z^{\rm model}$. The value of χ^2 per degree of freedom, χ^2_ν, is then calculated as

$$\chi^2_\nu = \sum_{i=1}^{N=9} \left(\frac{\left(\log Z_i - \log Z_i^{\rm model}\right)^2}{\left(\sigma_i^{\log Z}\right)^2 + \left(\sigma_i^{\rm int}\right)^2 + f' \left(\log M_*\right)^2 \left(\sigma_i^{\log M_*}\right)^2} \right) \frac{1}{N}, \tag{3}$$

where the sum runs over the nine ALMA [O III] 88 μm detections. In order to account for the uncertainties in the stellar mass estimates, we include a term in the variance that depends on the local derivative of the $Z(M_*)$ relationship with respect to the logarithm of stellar mass

Table 2. Summary of the reduced χ^2 test results. The columns specify the mass–metallicity constraints/forecasts discussed in this work, while the rows show varying $Z(M_*)$ models. The $z \sim 0$ and $z = 3.5$ cases are empirical relations from Maiolino 2008, while the $z = 6.0$ model is from the FIRE simulations of Ma 2016. The second and third columns correspond to the current constraints, while the remaining ones give forecasts in various scenarios (see text). The first entry in each cell is the (reduced) χ^2_ν value calculated following equation (3). The second entry specifies the corresponding p-value.

$Z(M_*)$ Relations	Jones 2020	Yang 2020	Max L_{21}/L_{10} ALMA	Mean L_{21}/L_{10} ALMA	Min L_{21}/L_{10} ALMA	Max L_{21}/L_{10} JWST	Mean L_{21}/L_{10} JWST	Min L_{21}/L_{10} JWST
$z \sim 0$	0.88, 0.49	1.23, 0.27	0.97, 0.46	1.08, 0.37	2.27, 1.5E-2	0.99, 0.45	1.08, 0.37	2.86, 2.2E-3
$z = 3.5$	0.55, 0.74	0.81, 0.61	2.81, 2.6E-3	1.99, 3.5E-2	1.50, 0.14	4.28, 1.39E-5	2.70, 3.8E-3	1.71, 8.1E-2
$z = 6.0$	0.38, 0.86	1.48, 0.15	2.85, 2.3E-3	2.12, 2.4E-2	1.71, 8.1E-2	3.97, 4.4E-5	2.61, 5.2E-3	1.83, 5.8E-2

(Clutton-Brock 1967), denoted above as $\hat{f}(\log M_*)$. This is calculated assuming the Ma 2016 $Z(M_*)$ relationship as $\hat{f}(\log M_*) = 0.35$.

The comparison with current constraints from Jones 2020 and Yang 2020 indicates that none of the mass–metallicity relationships in the literature are strongly favoured or disfavoured at the moment. Quantitatively, the χ^2_ν values for the example relationships in Fig. 3 are given in the first two columns of Table 2. The maximum χ^2_ν values for Jones 2020 and Yang 2020 are 0.88 and 1.23, respectively, corresponding to minimum p-values of 0.49 and 0.27, and so the current measurement errors are too large to distinguish models.

However, 52 μm measurements may help here, although the constraint obtained will depend on the gas densities in the target galaxies. Here, we only consider the additional metallicity constraints contributed by 52 μm measurements of the most promising targets: NB1006, B14, J0217, and J1211, as identified in Section 4. The top right panel of Fig. 3, for instance, illustrates that if the gas density in the four promising ALMA targets is large (so that L_{21}/L_{10} is near the maximal case identified in the previous section), the high metallicity implied in these galaxies would disfavour the simulated mass–metallicity relation in Ma 2016 and the higher redshift empirical fit from Maiolino 2008. That is, in this case, the data may prefer less redshift evolution in the normalization of the mass–metallicity relationship than in the AMAZE sample and in the FIRE simulations. On the other hand, in the minimal L_{21}/L_{10} scenario (bottom right) the lower redshift mass–metallicity relationships of Maiolino 2008 would be modestly disfavoured. In the intermediate case (lower left) the results may not strongly discriminate between any of the models shown.

In order to quantify these qualitative trends and our ability to constrain the mass–metallicity relationship with the upcoming 52 μm measurements, we calculate χ^2_ν between mock metallicity measurements in each scenario and the different empirical/simulation models. In computing χ^2_ν with equation (3) we use here the joint metallicity constraints from the current L_{10}/SFR and mock L_{21}/L_{10} measurements for NB1006, B14, J0217, and J1211, while we use the constraints from Yang 2020 for the other fixe ALMA [O III] 88 μm targets. The χ^2_ν test results are summarized in the fourth through sixth column in Table 2. Most notably, in the '$L_{21}/L_{10} = \max$' scenario, the χ^2_ν forecasts for the Maiolino 2008 $z = 3.5$ model and Ma 2016 $z = 6.0$ model are 2.81 and 2.85, respectively, corresponding to p-values on the order of 10^{-3}. That is, these cases would be strongly – if not decisively – disfavoured.

Furthermore, as discussed in Jones 2020, future JWST measurements of recombination lines such as Hα and Hβ should allow improved SFR determinations and dust extinction corrections. To gauge the improvements that may be possible, we suppose that the L_{10}/SFR measurement errors become dominated by $\sigma_{L_{10}}$ alone. In this case, the forecasted χ^2_ν values increase to 4.28 and 3.97 for the maximal mock [O III] 52 μm signal scenario, corresponding to p-values of 1.4×10^{-5} and 4.4×10^{-5}. That is, in this case, the high-redshift Maiolino 2008 and Ma 2016 models can be decisively excluded. The prospects in other scenarios are summarized in columns seven to nine of Table 2. In addition, JWST will be able to measure rest-frame optical emission lines from [O III] and [O II]. The [O III] optical lines are sensitive to the temperature of the emitting gas (e.g. Jones 2020 and Yang 2020) and so are likely less robust metallicity indicators on their own. However, in combination with the 88 and 52 μm transitions, the rest-frame optical [O III] and [O II] lines can help in empirically determining gas temperatures and ionization states. See Jones 2020 for further discussion. Hence the future combination of 52 μm and JWST SFR measurements should help in determining the mass–metallicity relationship during the EoR. It will also be important, however, to obtain a significantly larger sample of targets. In this context, galaxies with relatively low stellar masses, such as NB1006-2, seem especially interesting since measurements at the low-mass end will be valuable in determining the *shape* of the $Z(M_*)$ relationship at high redshift.

In the nearer term, these results suggest that the upcoming measurements will start to place interesting constraints on the evolution in the *normalization* of the $Z(M_*)$ relationship. Since the current data are consistent with a range of possibilities, from surprisingly little evolution – in comparison with even the $z \sim 0$ normalization from the AMAZE sample – to strong evolution (e.g. the current measurements are consistent with models below the Ma 2016 $z \sim 6$ normalization), it is perhaps premature to speculate on the precise implications in different scenarios. Instead, we only remark that the $Z(M_\star)$ normalization depends on the combined impact of evolving gas fractions, the efficiency of metal retention, and metal yields; it therefore provides a rich test of models of galaxy formation and feedback in a redshift regime well beyond that in which the models have been calibrated (e.g. Ma 2016; Torrey et al. 2019).

7 CONCLUSIONS

We have forecast the prospects for detecting the [O III] 52 μm emission line from the current sample of 10 ALMA [O III] 88 μm measurements towards galaxies at $6 < z \lesssim 9$. Adding 52 μm detections or upper limits will break the degeneracy between gas density and metallicity that remain from 88 μm and SFR measurements alone. Using the Yang 2020 model we forecast that the [O III] 52 μm lines from SXDF-NB1006-2, B14-65666, J0217-0208, and J1211-0118 can be detected within 10 h of on-source observing time, provided these galaxies have gas densities larger than $n_H \gtrsim 10^2$–10^3 cm^{-3}.

We forecast the parameter space improvements that will be possible for the four most promising targets, SXDF-NB1006-2, B14-65666, J0217-0208, and J1211-0118, with a 10 h ALMA 52 μm measurement. We find that the gas density constraint should tighten by 1–3 dex for these sources, while the metallicity posterior will narrow by as much as 1 dex for SXDF-NB1006-2, B14-65666, and

J1211-0118. We identify SXDF-NB1006-2 as the most favourable target for first follow-up observations. The 52 μm measurements will enable interesting constraints on the mass–metallicity relationship during the EoR, especially if these target galaxies have high gas densities. Further improvements are expected here following better SFR determinations from the JWST.

The 52 μm measurements should also help us understand the gas density of some of the first galaxies. These observations will help determine the internal structure of high-redshift galaxies and photon escape fraction in the sources that reionized the Universe.

ACKNOWLEDGEMENTS

AL acknowledges support through NASA ATP grant 80NSSC20K0497. We thank the referee for helpful suggestions, especially related to Section 6 of the manuscript.

DATA AVAILABILITY

The data used to support the findings of this study are available from the corresponding author upon request.

REFERENCES

Benson A., Venkatesan A., Shull J. M., 2013, ApJ, 770, 76
Binggeli C. et al., 2021, A&A, 646, A26
Carniani S. et al., 2017, A&A, 605, A42
Carniani S. et al., 2018a, MNRAS, 478, 1170
Carniani S., Maiolino R., Smit R., Amorín R., 2018b, ApJ, 854, L7
Clutton-Brock M., 1967, Technometrics, 9, 261
De Looze I. et al., 2014, A&A, 568, A62
Draine B. T., 2011, Physics of the Interstellar and Intergalactic Medium. Princeton University Press, Princeton, NJ
Ferland G. J. et al., 2017, Rev. Mex. Astron. Astrofis., 53, 385
Ferrara A., Vallini L., Pallottini A., Gallerani S., Carniani S., Kohandel M., Decataldo D., Behrens C., 2019, MNRAS, 489, 1
Harikane Y. et al., 2020a, ApJ, 896, 93
Harikane Y. et al., 2020b, ApJ, 896, 93
Hashimoto T. et al., 2018, Nature, 557, 392
Hashimoto T. et al., 2019, PASJ, 71, 71
Inoue A. K. et al., 2016, Science, 352, 1559
Jones T., Sanders R., Roberts-Borsani G., Ellis R. S., Laporte N., Treu T., Harikane Y., 2020, ApJ, 903, 150
Katz H. et al., 2019, MNRAS, 487, 5902
Kimm T., Cen R., 2014, ApJ, 788, 121
Kimm T., Blaizot J., Garel T., Michel-Dansac L., Katz H., Rosdahl J., Verhamme A., Haehnelt M., 2019, MNRAS, 486, 2215
Laporte N. et al., 2017, ApJ, 837, L21
Leitherer C. et al., 1999, ApJS, 123, 3
Lequeux J., Peimbert M., Rayo J. F., Serrano A., Torres-Peimbert S., 1979, A&A, 500, 145
Ma X., Kasen D., Hopkins P. F., Faucher-Giguère C.-A., Quataert E., Kereš D., Murray N., 2015, MNRAS, 453, 960
Ma X., Hopkins P. F., Faucher-Giguère C.-A., Zolman N., Muratov A. L., Kereš D., Quataert E., 2016, MNRAS, 456, 2140
Maiolino R. et al., 2008, A&A, 488, 463
Mancini M., Schneider R., Graziani L., Valiante R., Dayal P., Maio U., Ciardi B., Hunt L. K., 2015, MNRAS, 451, L70
Marrone D. P. et al., 2018, Nature, 553, 51
Moriwaki K. et al., 2018, MNRAS, 481, L84
Novak M. et al., 2019, ApJ, 881, 63
Pentericci L. et al., 2016, ApJ, 829, L11
Salpeter E. E., 1955, ApJ, 121, 161
Sanders R. L. et al., 2016, ApJ, 816, 23
Smit R. et al., 2018, Nature, 553, 178
Song M. et al., 2016, ApJ, 825, 5
Steidel C. C., Strom A. L., Pettini M., Rudie G. C., Reddy N. A., Trainor R. F., 2016, ApJ, 826, 159
Strom A. L., Steidel C. C., Rudie G. C., Trainor R. F., Pettini M., Reddy N. A., 2017, ApJ, 836, 164
Tamura Y. et al., 2019, ApJ, 874, 27
Torrey P. et al., 2019, MNRAS, 484, 5587
Tremonti C. A. et al., 2004, ApJ, 613, 898
Willott C. J., Carilli C. L., Wagg J., Wang R., 2015, ApJ, 807, 180
Yang S., Lidz A., 2020, MNRAS, 499, 3417

This paper has been typeset from a TEX/LATEX file prepared by the author.